JGR Atmospheres

RESEARCH ARTICLE
10.1029/2019JD031073

Aerosol-Cloud Interactions in Trade Wind Cumulus Clouds and the Role of Vertical Wind Shear

Takanobu Yamaguchi[1,2], **Graham Feingold**[2], **and Jan Kazil**[1,2]

[1]Cooperative Institute for Research in Environmental Sciences, University of Colorado, Boulder, CO, USA, [2]NOAA Earth System Research Laboratory, Boulder, CO, USA

Key Points:
- Large-eddy simulations show buffering of aerosol-cloud interactions in trade cumulus
- Wind shear enhances evaporation by tilting clouds, but protects cloud cores via clustering
- Charge-discharge cycles are correlated with cycles in the cloud size distribution

Correspondence to:
T. Yamaguchi,
tak.yamaguchi@noaa.gov

Citation:
Yamaguchi, T., Feingold, G., & Kazil, J. (2019). Aerosol-cloud interactions in trade wind Cumulus clouds and the role of vertical wind shear. *Journal of Geophysical Research: Atmospheres*, *124*, 12,244–12,261. https://doi.org/10.1029/2019JD031073

Received 3 JUN 2019
Accepted 22 OCT 2019
Accepted article online 8 NOV 2019
Published online 24 NOV 2019

Abstract In shallow cumulus clouds, cloud deepening as a dynamical response to increased droplet number concentration has recently been shown to buffer the microphysical suppression of precipitation. In the current study, large eddy simulations with a two-moment bin microphysics model are employed to revisit this buffering and to investigate the role of vertical wind shear in aerosol-cloud interactions in trade wind cumuli. An idealized case is developed based on ship measurements and corresponding reanalysis data over the Sulu Sea in the Philippines in September 2012. A quasi-steady state is reached after roughly 25 – 35 hr for all six simulations performed (three different aerosol concentrations covering 35 – 230 cm^{-3}, with/without vertical wind shear). All simulations show that the aerosol effect is buffered, to first order; increased aerosol results in deeper clouds, a reduced cloud fraction, and an increase in the shortwave cloud radiative effect. For the no-shear cases, positive aerosol perturbations result in a small increase in surface precipitation, while the opposite is true in the presence of vertical wind shear because of muted deepening. Analysis shows competing influences of vertical wind shear; enhanced cloud clustering protects clouds from evaporation and entrainment while tilting of clouds enhances evaporation. In spite of the small responses of surface precipitation to very large changes in aerosol, cloud size and spatial distributions and charge/discharge precipitation cycles differ significantly, expressing changes in the pathways to surface precipitation and a dynamical buffering of the system.

1. Introduction

A decade ago, Stevens and Feingold (2009) hypothesized that shallow (liquid) cloud systems tend to have a muted response to aerosol perturbations, both in terms of effects on cloud brightening and on precipitation formation. They described these systems as "buffered," in the sense that when perturbed, internal adjustments in the system counteract the expected response. The intervening years have shown that buffering with respect to aerosol perturbations is commonplace, albeit with exceptions — for example, when reductions in aerosol through coalescence scavenging lead to a runaway reduction in stratocumulus cloud amount. In the case of shallow cumulus, both observational (Koren et al., 2014, and references therein) and high-resolution large eddy simulation (LES) studies (e.g., Seifert et al., 2015; Dagan et al., 2017) have demonstrated that clouds deepen in response to increases in aerosol and that this deepening can offset and even overwhelm microphysical suppression of rain formation. Microphysically, increases in the aerosol concentration in a shallow cumulus field suppress droplet growth and brighten these clouds through the cloud albedo effect (Twomey, 1977). The enhanced evaporative cooling and moistening in the free troposphere allow subsequent clouds to deepen, increasing the potential for precipitation, and reductions in cloud amount. Dynamical adjustments such as these illustrate the non-linear responses to aerosol perturbations and the imprudence of simply assuming that increases in the aerosol result in brightening (Twomey, 1977) and precipitation suppression (Albrecht, 1989). For example, Seifert et al. (2015, hereafter S15) showed that in the precipitating trade wind cumulus regime, the cloud lifetime effect (Albrecht, 1989) is to first order insensitive to aerosol amount. Nevertheless, the frequency and extent to which shallow cloud systems are buffered is not well-established (e.g., Boucher et al., 2013; Mülmenstädt and Feingold, 2018). Buffering could potentially be a strong constraint on radiative forcing associated with aerosol-cloud interactions, motivating us to explore this question here.

This study examines aerosol-cloud interactions in trade cumulus cloud fields in the Philippine regions with LES. The Philippine region is selected to support the NASA Cloud, Aerosol, and Monsoon Processes Philippines Experiments ($CAMP^2Ex$) field campaign. The frequent aerosol intrusions from local and regional

pollution sources provide an interesting alternative to the more commonly studied Caribbean trade-wind region. A new case study is developed based on ship measurements carried out in 2012. In addition, the role of vertical wind shear, alone and in combination with aerosol perturbations, is investigated; to our knowledge, only a small number of studies have discussed the influence of vertical wind shear on shallow cumulus clouds, in contrast to the large body of literature that exists for deep convective clouds (e.g., Houze, 2018). The effect of wind speed on shallow cumulus development is also limited. For instance, Nuijens and Stevens (2012) used LES to show that trade cumulus deepen in response to increasing wind speed.

Malkus (1952) showed that shallow cumulus clouds become more tilted with stronger vertical wind shear. She derived an equation for the slope of shallow cumulus clouds and applied it to time lapse photographs. The results indicate that clouds evaporate more readily as wind shear becomes stronger because of increasing interaction with dry air. When wind shear is weak, the clouds remain nearly vertical, and newly formed clouds can grow into and entrain air moistened by their predecessors; in contrast, under strong wind shear, dissipating clouds become tilted aloft, and new clouds, which grow more vertically, tend to penetrate dry air. She also noted "... even the microphysics of clouds, drop-growth rates and size distributions, may be expected to be markedly influenced by such macroscopic external variables as wind shear." Asai (1964) performed numerical simulations of non-precipitating shallow convection with and without vertical wind shear for a shallow (5 km) domain depth and showed that vertical wind shear suppresses convection due to both the transformation of eddy kinetic energy into mean kinetic energy and the weakness of the transformation of potential energy into kinetic energy. Neggers et al. (2003) showed that the projected cloud area becomes a little larger and the slope (in logarithmic space) of the power law cloud size distribution decreases as wind shear increases. They attributed these changes to cloud tilting. Brown (1999) also showed a slight increase in cloud fraction with increasing wind shear. These studies suggest that vertical wind shear weakens convection, enhances cloud evaporation, and to a certain extent, increases cloud fraction. Describing the interplay between wind shear and aerosol-cloud interaction is therefore another focus of this study.

Trade wind cumuli tend to organize in open cellular structures as a response to cold pools formed by cool, dry penetrative downdrafts generated via evaporation of precipitation (Zuidema et al., 2012; Zuidema et al., 2017). Moistening of the downdrafts aids subsequent convection at the moist edges of the cold pools (Tompkins, 2001; Seifert and Heus, 2013) and/or by dynamical lifting and moisture convergence in the interacting cold pool outflows (Xue et al., 2008). Following the theory for deep convective clouds, Li et al. (2014) discuss a possible influence of environmental wind shear on propagation of the outflow for trade cumulus cold pools; the ambient shear can tilt updrafts away from the propagating cold pool, which strengthens the secondary convection. It can also facilitate precipitation and evaporation inside of the cold pool, which strengthens the cold pool. In their simulations of the transition from shallow-to-deep convection Schlemmer and Hohenegger (2014) show that wind shear results in the development of large clouds and suggest a positive feedback for the cold pool dynamics; large cold pools result in large moist areas, which spawns large clouds. Combining these insights, it is plausible that vertical wind shear tends to cluster clouds in the precipitating trade wind cumulus system.

A description of our LES model is presented in the next section, and a new trade wind cumulus case in section 3. Results are shown in section 4, and section 5 summarizes and concludes the study.

2. LES Model

The System for Atmospheric Modeling (SAM) (Khairoutdinov and Randall, 2003) is employed as an LES model. SAM solves the anelastic system of equations using the finite difference approximation formulated on the Arakawa C grid with a height coordinate. Velocity components are predicted using the third-order Adams-Bashforth scheme (Durran, 1991) and the second order center advection scheme, while scalars (liquid water static energy, subgrid scale turbulence kinetic energy, and prognostic microphysical variables) with the forward in time, monotonic fifth-order advection scheme of Yamaguchi et al. (2011). Diffusion is explicitly computed with eddy viscosity based on Deardorff (1980). Surface fluxes are computed based on Monin-Obukhov similarity (Monin and Obukhov, 1954). For the present study, horizontal (vertical) grid spacing is 100 (40) m. The domain size is $48 \times 48 \times 6$ km. The time step is 2 s, and duration of all simulations is 60 hr.

Radiation is computed every minute with the Rapid Radiative Transfer Model (RRTMG) (Mlawer et al., 1997; Iacono et al., 2008). Because the domain top is capped at 6 km, we account for the radiative effects of the

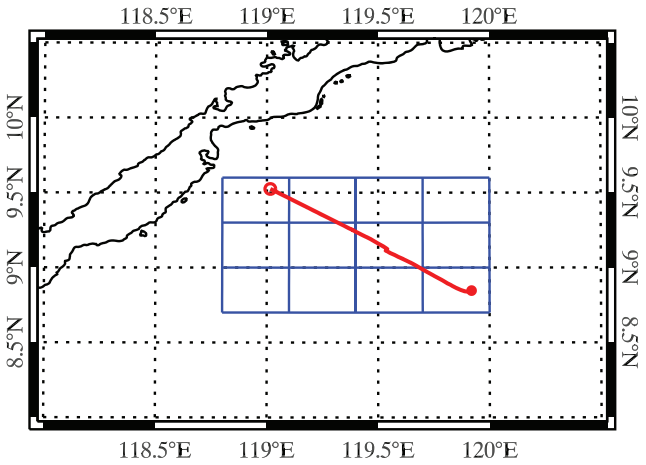

Figure 1. Ship trajectory (red line) on September 21, 2012 during the 7SEAS campaign. The trajectory starts at the open red circle and ends at the filled red circle. The 12 blue grid boxes are locations of the ERA5 data used to generate soundings.

atmosphere over a much deeper layer of the atmosphere by extending the initial temperature and water vapor profiles from the domain top to the top of atmosphere based on ERA5 reanalysis data. The extended profiles are smoothly connected to the initial profiles to minimize biases in radiation calculations with RRTMG.

Microphysical processes are computed with the Tel Aviv University (TAU) two-moment bin microphysics model (Tzivion et al., 1987; Feingold et al., 1996). The size distribution is divided into 33 bins with mass doubling from one bin to the next. The smallest droplet radius is 1.56 μm. Unique to the TAU scheme is that prognostic equations for both mass mixing ratio and number concentration of drops are solved. While the number of advected scalars is double that of typical (mass doubling) bin microphysical schemes, early tests showed that a single moment bin scheme requires three times the number of bins to achieve the same accuracy as a double moment bin scheme (Tzivion et al., 1987).

Activation of aerosol is based on predicted ambient supersaturation (Clark, 1974). The aerosol is assumed to have a lognormal size distribution with a geometric mean radius of 0.2 μm and a geometric standard deviation of 1.5. Condensation and evaporation are computed via vapor diffusion to/from drops using the method of Stevens et al. (1996). Collection processes are based on Tzivion et al. (1987) and breakup processes on Feingold et al. (1988). The collection kernels knit together collision efficiencies after Hall (1980) as well as coalescence efficiencies for drizzle (Ochs et al., 1986) and raindrops (Low and List, 1982a). In the rain drop regime where drops are unstable enough to be able to breakup as a result of binary collisions, the breakup efficiency is assumed to be 1 minus the coalescence efficiency. Details of the breakup kernel parameterization are in Low and List (1982b). As is customary, drop fall velocities are represented by piece-wise power law functions with fall velocity dependence on radius changing from r^2 to r to $r^{1/2}$ to a constant as drops increase in size from small droplets through drizzle drops and raindrops. Drop sedimentation is computed with a first-order upwind scheme. For purposes of diagnosis, a droplet radius of 25 μm is used to demarcate cloud water from drizzle/rain water.

Changes have been made to our standard method of advecting water species. The total mass mixing ratio (sum of vapor and condensate) and total number concentration (sum of aerosol and drops) are predicted so that the water vapor mixing ratio and aerosol number concentration are diagnostic variables. This implementation implicitly maintains the budget of both mass mixing ratio and number concentration through condensation/evaporation, collection/breakup, and regeneration of aerosol. One caveat of this implementation is that aerosol number concentration may become negative after advection due to the nonlinear nature of monotonic high-order scalar advection schemes, which can not exactly maintain the linear relationship between scalars (Ovtchinnikov and Easter, 2009; Morrison et al., 2016), 2009; Morrison et al., 2016). In this case, before computing microphysics, aerosol number concentration is set to zero after droplet number concentration in each bin is reduced by scaling it with a proportional factor given as $1 + \frac{N_a}{N_d}$ where N_a is aerosol number concentration (negative value) and N_d is total droplet number concentration (i.e., sum of all number concentration bins).

3. Idealized Trade Cumulus Case

S15 simulated the RICO LES intercomparison case (van Zanten et al., 2011) with a large domain (51.2 km), high resolution (25-m grid spacing), long duration (60 hr), a two-moment bulk microphysics scheme (albeit with a spatiotemporally fixed drop concentration and saturation adjustment), interactive radiation code, and interactive surface flux calculation. S15 found that the system reaches a quasi-steady state earlier when radiation is interactively computed, compared with simulations with a specified radiative heating rate.

Here a new idealized trade cumulus case is developed in order to test responses to aerosol and vertical wind shear for a different subtropical trade wind cumulus region. The case is based on a ship measurement during the 7 Southeast Asian Studies (7SEAS) in 2012 (Reid et al., 2016). Based on personal communication

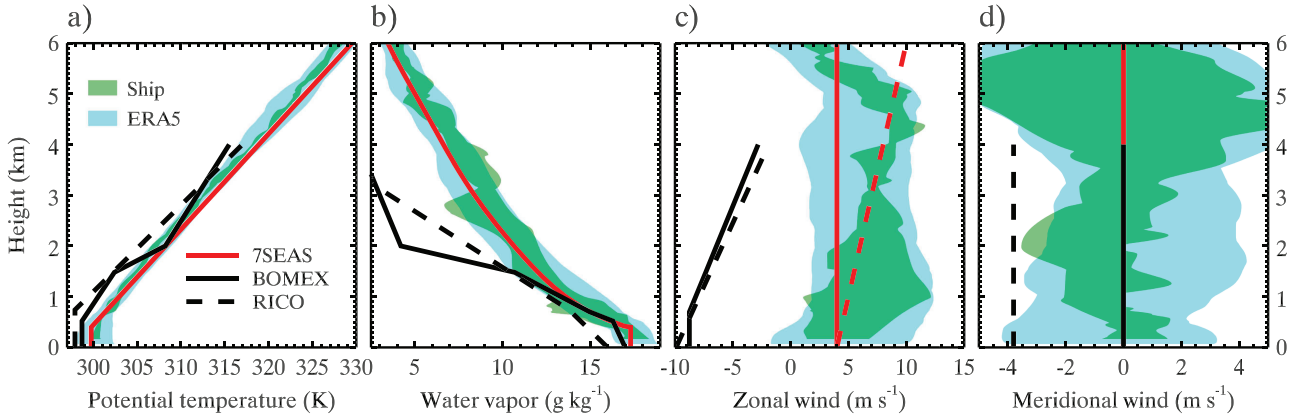

Figure 2. Profiles of θ, q_v, u, and v used for the idealized 7SEAS case (red solid line) as well as the BOMEX (black solid line) and RICO (black dashed line) cases superimposed on the shading for the ship data (green) and ERA5 (light blue). The shading covers minimum and maximum values over a 24-hr period for both data sets. The ship measurements took place every 6 hr (four profiles per day for each variable). For hourly ERA5 data, the 12 grids of the ERA5 global domain shown in Figure 1 are used (total of 288 profiles). Two types of zonal wind are used for this study: one without vertical wind shear, the other with vertical wind shear (red dashed line).

with J. Reid (including photographs), we selected a cruise in the Sulu Sea, Philippines, which took place on September 21; the ship track is indicated as the red line from the open circle to the filled circle in Figure 1.

Vertical profile data (zonal and meridional winds, u and v respectively; potential temperature, θ; and water vapor mixing ratio, q_v) are available every 6 hr and are plotted in Figure 2 as a translucent green shading, which covers the minimum and maximum at each level. In order to generate smooth, representative soundings, the hourly ERA5 data sampled at the 12 blue grids shown in Figure 1 are used (translucent light blue shadings in Figure 2). ERA5 is the most recent reanalysis product generated by the European Centre for Medium-Range Weather Forecasts and is obtained via the Copernicus Climate Change Service (C3S) Climate Data Store. Both the ship soundings and ERA5 soundings are in reasonable agreement. The ERA5 data are space- and time-averaged and then interpolated to a 20-m vertical mesh up to 7 km. After some test simulations, the θ profile is idealized as a constant 299.76 K below 400 m (subcloud mixed layer) and a linearly warming profile that gives 329.5 K at the 6-km domain top. The q_v profile above 400 m is idealized with a seventh-order polynomial, that is, $q_v = \sum n = 0^7 c_n z^n$, with the coefficients $c_n \approx \left\{21.88, -1.601 \times 10^{-2}, 1.255 \times 10^{-5}, -6.424 \times 10^{-9}, 1.920 \times 10^{-12}, -3.279 \times 10^{-16}, 2.959 \times 10^{-20}, -1.093 \times 10^{-24}\right\}$ obtained from the fit to the data above 400 m. For the subcloud mixed layer, that is, below 400 m, the vertically averaged ERA5 value, 17.31 g kg^{-1}, is used. Two types of u profiles are used: a surface wind of 4 m s^{-1} *without* vertical shear (the C cases) and *with* vertical wind shear of 0.001 s^{-1} (the S cases). The surface wind speed and vertical shear are approximated from the ship measurements. A zero v profile is used for simplicity. These profiles are shown in Figure 2 as a red line and also given in Table 1. Relative to the two LES intercomparison cases of BOMEX (black solid lines) (Siebesma et al., 2003) and RICO (black dashed lines), the new 7SEAS case is warmer and significantly moister, but with similar wind shear.

Table 1
Initial profile and large-scale forcings

	Initial profiles				Large-scale forcings		
Height	θ	q_v	u	v	W	$\left.\frac{\partial\overline{\theta}}{\partial t}\right\|_V$	$\left.\frac{\partial\overline{q_v}}{\partial t}\right\|_V$
(m)	(K)	(g kg^{-1})	(m s^{-1})	(m s^{-1})	(cm s^{-1})	(K d^{-1})	(g kg^{-1} d^{-1})
0	299.76	17.31	4, 4	0	0	−0.944	−0.991
400	299.76	17.31	–	–	−0.5	–	–
4000	–	–	–	–	–	–	0.701
6000	329.50	–	4, 10	0	−0.5	−0.944	0.701

Note. At levels where no entries are filled, values are linearly interpolated with the surrounded values except q_v above 400 m, which is constructed with a seventh order polynomial with the coefficients provided in the text. Both wind speed for the C case without vertical wind shear and the S case with shear are listed for u.

The time-independent large-scale forcing given in Table 1 is specified in the following manner. First, a quasi-steady state is assumed so that the budget equation for horizontal mean θ can be written as

$$\frac{\partial\overline{\theta}}{\partial t} = \left.\frac{\partial\overline{\theta}}{\partial t}\right|_R + \left.\frac{\partial\overline{\theta}}{\partial t}\right|_W + \left.\frac{\partial\overline{\theta}}{\partial t}\right|_V + \left.\frac{\partial\overline{\theta}}{\partial t}\right|_C \approx 0 \quad , \tag{1}$$

where the overbar denotes horizontal mean, the subscript R represents the tendency due to radiation, W due to large-scale vertical velocity, V due to large-scale horizontal velocity, and C due to convection (representing the simulated dynamical and microphysical processes). The budget equation for $\overline{q_v}$ can be written in the same manner. For the upper part of the domain, where the influence of convection is much smaller than other processes, the $\overline{\theta}$ budget equation can be approximated as

$$\left.\frac{\partial\overline{\theta}}{\partial t}\right|_V + \left.\frac{\partial\overline{\theta}}{\partial t}\right|_R + \left.\frac{\partial\overline{\theta}}{\partial t}\right|_W \approx 0 \quad . \tag{2}$$

In order to avoid complexity in configuring large-scale forcings, the RICO case is consulted: i) the total tendency of R and V for θ is assumed constant with height, ii) the V tendency for q_v is constant and positive (moistening) at and above a specified height, decreasing linearly to a negative (drying) value from that level to the surface, and iii) W is set to -0.5 cm s^{-1} at and above a specified height and linearly changes to zero from that level to the surface. An additional simplification is made so that the R tendency and V tendency for θ are constant with height. This constant R tendency is only used to configure large-scale forcings; radiation is interactively computed during simulations. The constant R tendency is assessed by computing radiative heating rates offline based on the initial thermodynamic profile. The W tendencies for θ and q_v are also computed offline with the initial profile. With (2), the V tendencies for θ and q_v are obtained for the upper part of the domain. Convection influences the middle and lower parts of the domain; its influence is, however, unknown and it is also affected by the other tendencies. In order to generate a set of large-scale forcings that satisfy (1), simulations are iteratively run by adjusting large-scale forcings (R tendency, lowest level of constant W, and V tendency for θ and q_v). (For this iterative procedure, a simple microphysics scheme (Khairoutdinov and Kogan, 2000) is used due to the large computational cost of the TAU two-moment bin scheme.) For each iteration, $\overline{\theta}$ and $\overline{q_v}$ are compared against their initial profile and adjustments are made manually. The final tuned value of the R tendency is -1.35 K d^{-1}; the lowest level of the constant W is 400 m; $\left.\frac{\partial\theta}{\partial t}\right|_V = -0.944$ K d^{-1} for all levels; $\left.\frac{\partial q_v}{\partial t}\right|_V = 0.701$ g kg^{-1} d^{-1} above 4 km and decreases linearly to -0.991 g kg^{-1} d^{-1} at the surface.

Other specifications are as follows. The sea surface temperature is set to 303.5 K and the surface pressure to 1009.6 hPa, derived from 24-hr average ship measurements (sampled every minute). The mean horizontal wind is nudged toward the initial condition with a 1-hr time scale in order to maintain vertical wind shear. The horizontal mean total number concentration is nudged with a 1-hr time scale to the initial aerosol concentration in order to prevent significant depletion of aerosol by microphysical processes. (Locally strong reductions due to wet scavenging are represented.) Neither the Coriolis force nor a diurnal cycle is included; radiation is computed with a diurnally averaged insolation at 8.98° N and 119.73° E, which is the 24-hr mean location of the ship track. In order to minimize numerical errors and diffusion associated with advection, the model domain is translated at 4 m s^{-1} in the zonal direction. Turbulence is damped above 5 km up to the domain top at 6 km. Finally, the initial perturbation follows the RICO case.

For both C (without vertical wind shear) and S (with vertical wind shear) cases, three initial aerosol concentrations are simulated: 35, 150, and 230 mg^{-1}. These six simulations are henceforth referred to as C035, C150, C230, S035, S150, and S230.

Model output analyzed in this study such as one-dimensional time series, horizontally averaged profiles, and two-dimensional variables (e.g., liquid water path, cloud top height) consist of snapshots every minute.

4. Results

4.1. Buffering of Aerosol Effect in Quasi-Equilibrium State

Figures 3 and 4 show the cloud albedo field with color shadings for two ranges of rain rates every 15 hr, for all six cases; heavy drizzle and light rain (12– 60 mm day^{-1}) is in red and moderate rain (>60 mm day^{-1}) is in green. Cloud albedo is computed from optical depth of total condensate (cloud and drizzle/rain) with the

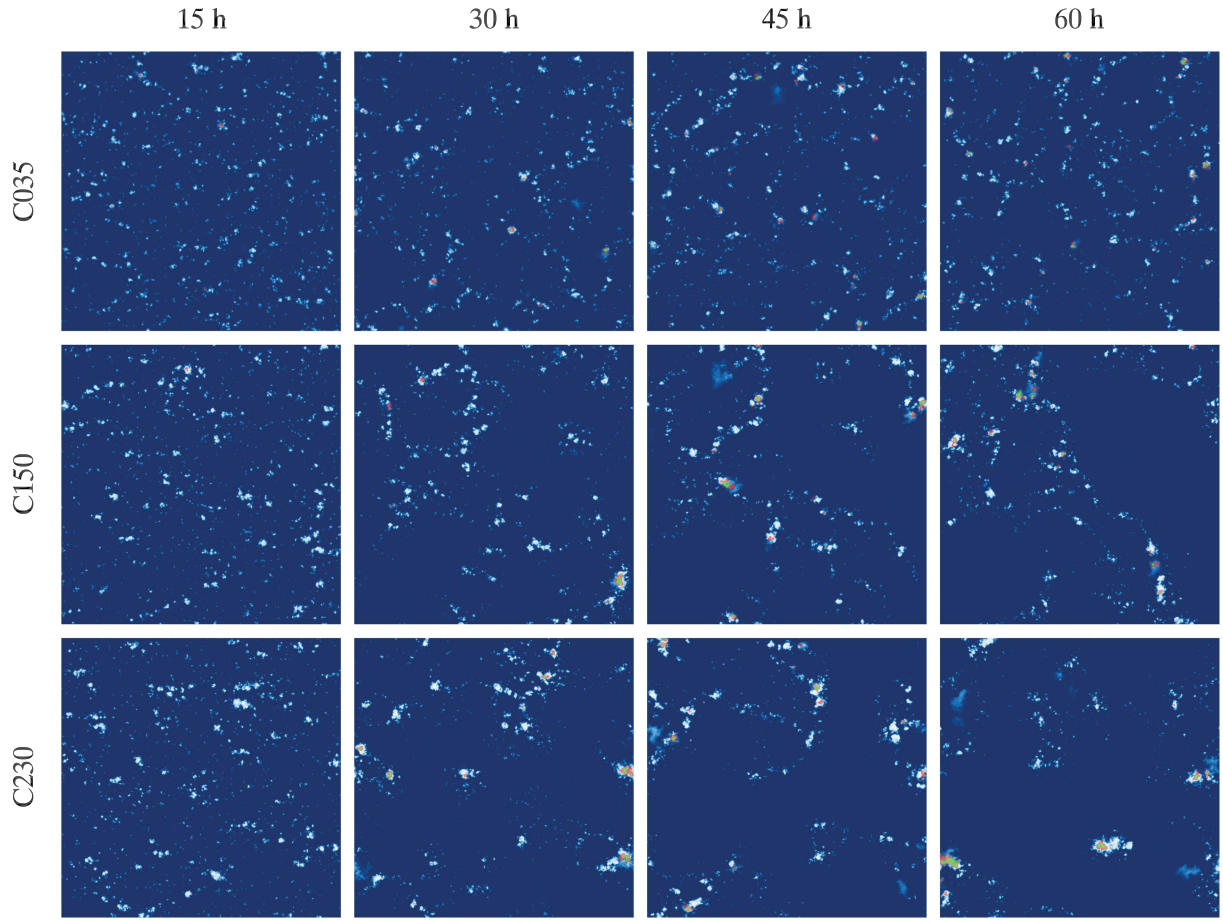

Figure 3. Cloud albedo every 15 hr for the C cases (without wind shear). Heavy drizzle and light rain, between 12 (0.5 mm hr^{-1}) and 60 mm day^{-1} (2.5 mm h^{-1}), are shown with red shading, and rain greater than 60 mm day^{-1} is shown with green shading.

two-stream approximation of Bohren (1987). In the absence of wind shear (Figure 3), a cellular structure emerges, and with time, larger cells and cloud clusters begin to appear for the more polluted cases. Wind shear (Figure 4) distorts the cellular structure, that is, the cells are elongated parallel to the mean wind direction, $(\overline{u}, 0)$. For both C and S simulations, larger cells, mostly devoid of clouds and cloud clusters appear for the more polluted cases. Interestingly, the wind shear produces larger cells compared to the corresponding cases without wind shear, especially for the clean cases (S035 and C035).

Figure 5 shows the hourly averaged time evolution of selected variables. Horizontal mean is applied for inversion height (z_i), liquid water path (L_w; summation of cloud and rain water), cloud water path (L_c), and surface rain rate (R_{sfc}) while other variables such as maximum cloud top height ($z_{c,max}$), cloud fraction (f_c), and cloud droplet number concentration (N_c) are computed with conditional sampling of cloudy grids; we use a cloud water mixing ratio greater than 0.01 g kg^{-1} to define cloud. Wind shear generally adds more variability (i.e., larger amplitudes and more oscillatory behavior), and S230 has a large precipitation event around 27 hr. The period to reach a quasi-equilibrium state differs among the cases; clean cases require a shorter period than polluted cases. S230 especially takes a prolonged time due to the intense precipitation event at 27 hr. For these time series, 25 to 35 hr is required for all simulations to reach a quasi-steady state. S15 used R_{sfc} and f_c to deduce the time required to achieve a quasi-steady state. Here, in order to have the same sample duration for all simulations, model output over the last 20 hr is used for the following analyses and discussion.

Table 2 lists the last 20-hr mean of selected variables (time series of N_c, $z_{c,max}$, z_i, f_c, L_w, and R_{sfc} are also shown in Figure 5). The range of N_c is a little larger than that used in S15 ($N_c \in \{35, 50, 70, 95\}$ cm^{-3}). Consistent with S15, clouds deepen as N_c increases for both the C cases and the S cases. These simulations show a clear

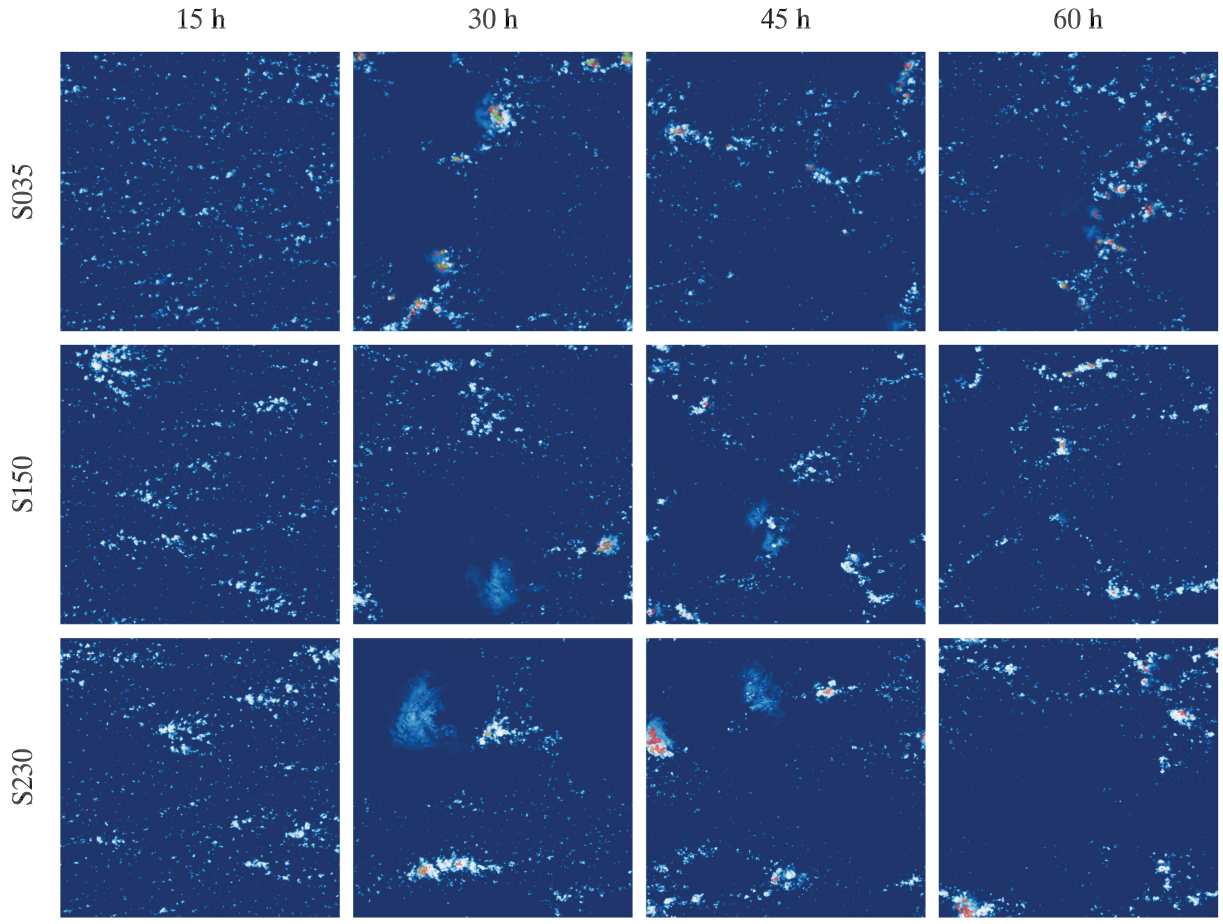

Figure 4. Same as Figure 3 but for the S cases (with wind shear). The mean horizontal wind direction is from left to right.

but weak trend in f_c, which decreases as N_c increases. For the C simulations, an increase in initial aerosol number concentration (N_a) results in small increases in L_w and R_{sfc} showing that microphysical suppression of rain is more than compensated by enhancement of rain due to deepening. Both effects combine to enhance the shortwave cloud radiative effect (SWCRE), $\sim$ 0.86 W m^{-2}. In the S cases, deepening is weaker, and L_w and R_{sfc} decrease so that microphysical suppression of rain dominates, and the enhancement of SWCRE is smaller, $\sim$ 0.74 W m^{-2}. However SWCRE is higher than for the C cases primarily due to higher f_c (discussed below) and to some extent because of higher N_c. Trends in z_i follow those of $z_{\mathrm{c,max}}$ but with a saturation at $N_a = 150$ mg^{-1}.

As mentioned above, Table 2 shows that in both C and S cases there is a weak but systematic reduction in f_c in response to increasing N_a. Considering the same N_a (or similar N_c), wind shear produces slightly higher f_c than the cases without wind shear, consistent with Neggers et al. (2003) and Brown (1999). These studies showed a small increase in f_c in response to prescribed wind shear based on BOMEX, a case with some similarities to the current study. A several % increase in f_c was achieved when shear was doubled in Neggers et al. (2003) while Brown (1999) obtained $\sim$ 1 % increase in f_c for doubled wind shear. Note that the f_c for BOMEX is typically around 13 % (Siebesma et al., 2003).

Overall, the effects due to wind shear and a factor 6.5 increase in aerosol are relatively muted. It is, however, worth exploring the underlying processes that produce these modulations.

4.2. Compensation Between Vertical Wind Shear Effects as Manifested in Cloud Field Properties

The power law is widely used to represent cloud size distributions (CSDs) and even more widely used to represent scale-invariance and multiplicative processes in a host of natural systems (Newman, 2005). Here we apply the power law as a tool to quantify the slope of CSDs in log-log space, for ease of comparison between cases, and without attachment to any deeper meaning. CSDs are calculated based on the two-dimensional

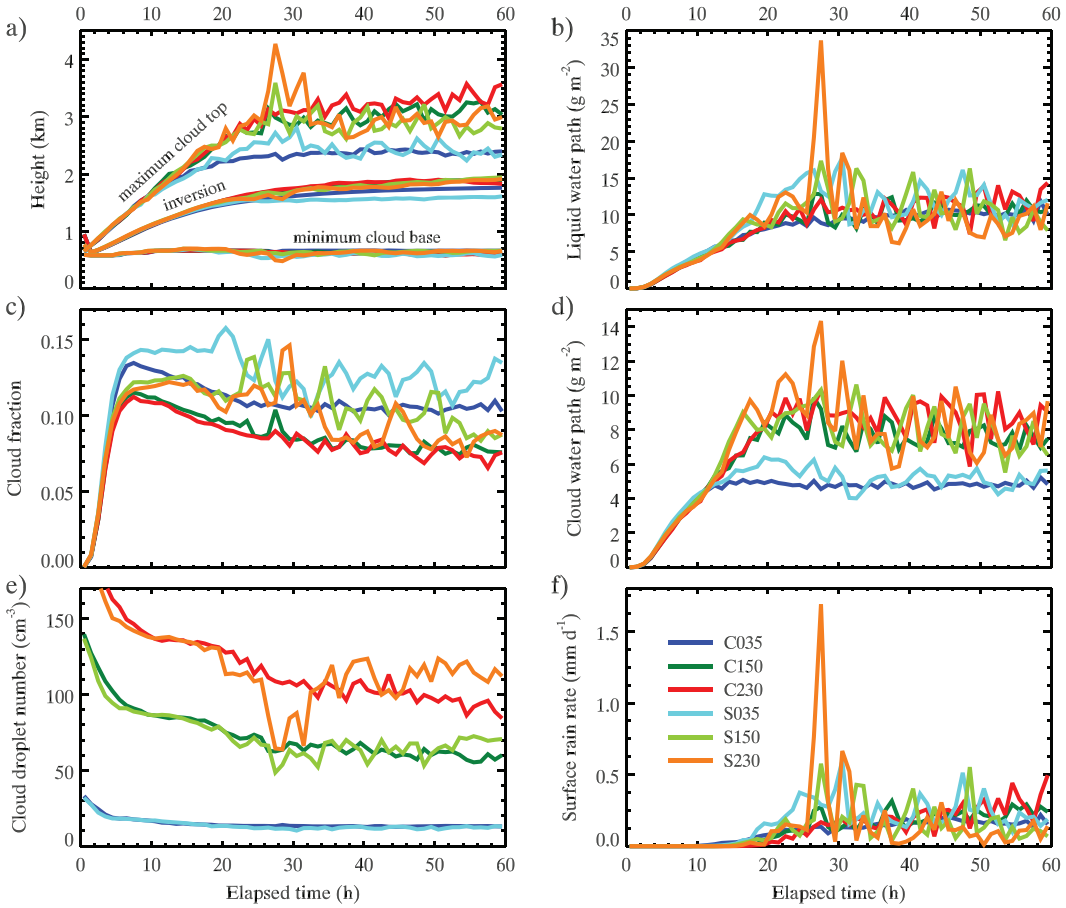

Figure 5. Hourly mean time series for selected variables. A grid box is defined as cloudy when the cloud water mixing ratio exceeds 0.01 g kg^{-1}. This definition is used for diagnosing maximum cloud top and minimum cloud base height, (projected) cloud fraction, and cloud droplet number concentration. Inversion height is defined as the maximum gradient of potential temperature. Liquid water path includes all condensate — cloud plus rain.

areal projection of the L_w field using raw (100 m) grid-spacing, without any binning. A common concern with poor sampling at the tail (large) end of a negative power law is alleviated here by using a large domain (48 × 48 km, similar to that of Neggers et al. (2019), who showed cloud size distributions converging at 51.2 km for a single snapshot of a cloud field) and sampling over a long period of time (20 hr at 10-min intervals, or 120 samples; see caption to Figures 6 and 7 below for quantification of large-cloud samples). Because a single power law fit is typically inadequate over the full range of sampled clouds, we apply two fits that together yield information on the relative contributions of small and large clouds: one power law fit to *all* clouds and a second to clouds with projected area *less than* 1 km^2. Neither is a good fit to the entire population, but together, they are a useful means to interpret evolution in CSDs.

The mechanical influence of wind shear promotes tilted clouds (Malkus, 1952), which results in a larger projected cloud area and this should contribute to a decreased slope (in logarithmic space) of the power law fit to the CSD (Neggers et al., 2003). The CSD for the six cases (Figure 6) along with the snapshot images (Figures 3 and 4) backs this up. For these CSDs, the wind shear cases clearly generate horizontally larger clouds compared with their counterparts without wind shear, and their slopes are gentler when all clouds are included (red lines). The slopes are steeper for the wind shear cases when only smaller clouds (less than 1 km^2; green lines) are analyzed. Note that higher aerosol concentrations result in a steeper slope for the small cloud population and a gentler slope for all clouds. Thus, wind shear and aerosol loading modulate the CSD in the same direction; however, wind shear imparts a greater effect. This modulation is achieved by transferring clouds with their area between ~ 0.3 and 1 km^2 to larger clouds in the distribution so that the field contains larger clouds with, to first order, similar projected cloud fraction (Table 2). For the

Table 2
Last 20-hr mean of selected variables

Case	N_c (cm^{-3})	$z_{c,max}$ (km)	z_i (km)	f_c	$f_{c,base}$	L_w ($g\ m^{-2}$)	R_{sfc} ($mm\ d^{-1}$)	SWCRE ($W\ m^{-2}$)
C035	13.1	2.38	1.73	0.105	0.045	10.2	0.17	−6.22
C150	60.3	3.10	1.87	0.078	0.031	10.5	0.22	−6.61
C230	97.2	3.30	1.88	0.076	0.029	11.8	0.27	−7.08
S035	12.2	2.42	1.58	0.124	0.046	11.9	0.24	−7.02
S150	65.7	2.87	1.88	0.099	0.034	10.4	0.16	−7.79
S230	112.9	2.95	1.83	0.087	0.033	9.50	0.11	−7.76

Note. N_c is cloud droplet number concentration, $z_{c,max}$ is maximum cloud top height, z_i is inversion height, f_c is projected cloud fraction, $f_{c,base}$ is cloud fraction at the cloud base, L_w is liquid water path (cloud plus rain), R_{sfc} is surface rain rate, and SWCRE is shortwave cloud radiative effect, that is, $(F^{\downarrow}_{all} - F^{\uparrow}_{all}) - (F^{\downarrow}_{clear} - F^{\uparrow}_{clear})$, where F is SW flux at the top-of-atmosphere.

S simulations, physically this transfer is associated with tilting clouds, clustering of clouds (i.e., generation of broader clouds), and the formation of larger cellular structures (Figures 3 and 4).

When considering the response of CSDs to an increase in aerosol loading, Xue and Feingold (2006) also noted an increasing concentration of small clouds in shallow, weakly to non-precipitating cumulus (BOMEX), attributing it to enhanced cloud edge evaporation. Jiang et al. (2009) saw both an increasing concentration of small clouds and a preponderance of large clusters for more heavily precipitating RICO simulations. They did not comment on the larger clusters. Cloud clustering in response to increases in aerosol may be attributed to microphysical suppression followed by intense precipitation associated with deepening. It may also be a result of drier downdrafts associated with deepening and outflows that have to travel farther before they become conditionally unstable (Vogel et al., 2016). The raw, 1-min interval R_{sfc} for the C cases clearly shows stronger precipitation with increased N_a (not shown; c.f., Figure 5f). The strong precipitation generates stronger outflows, which tend to create large clear areas and convergence points that are farther away. Enhanced cloud clustering by wind shear is consistent with Schlemmer and Hohenegger (2014), albeit in deep cumulus. How the applied wind shear enhances cloud clustering (c.f., Li et al., 2014) is an important research question, which we defer, however, to future research.

In Table 2, cloud base cloud fraction ($f_{c,base}$) follows the f_c trend in terms of aerosol loading and with/without wind shear. Of note is the increased $f_{c,base}$ with wind shear for given N_a. Figure 7 shows the *cloud base* size distribution (CBSD), created with all clouds identified for Figure 6. The change in slope due to wind shear as well as aerosol loading is in the same direction as that for the CSD discussed just above. By comparing CSD and CBSD for each case, the slopes computed from only smaller clouds (area less than 1 km^2) are generally similar, while the slopes computed from all clouds are gentler for the CSD than the CBSD. The average change in the magnitude of the slope from CBSD to CSD for all clouds for the six cases is 0.32 with minimum of 0.25 (C035) and maximum of 0.41 (S150). Sheared cases already exhibit substantial clustering at cloud base, and the flattening of slopes in log-log space with increasing altitude is an indication of the effects of tilting and anvil formation on projected cloud area. In the non-shear cases, the flattening of slopes with increasing altitude is primarily due to anvil formation.

Wind shear broadens CSD by tilting and clustering. When these two effects are considered separately, they impose competing effects on cloud development. According to Malkus (1952) and Asai (1964), tilting increases exposure to the environment, which amplifies evaporation and results in weaker updrafts and shallower cloud tops. Cloud fraction near cloud top becomes larger, and precipitation generation is reduced. Clustering, on the other hand, creates wider clouds, whose cores are more protected, thus leading to higher cloud tops. Cloud fraction near cloud base becomes larger (Table 2). The elevated cloud top is also subject to an additional compensation when the cloud contains large enough condensate to form drizzle/rain, which tends to suppress vertical development. We hypothesize that for the vertical wind shear applied to our simulations, these three effects compensate one other so that the net effect of wind shear is relatively small.

The subtle, yet detectable differences among the simulations due to the wind shear seen in Table 2 can be explained with these three effects. According to Table 2, for the polluted cases (C230 and S230), wind

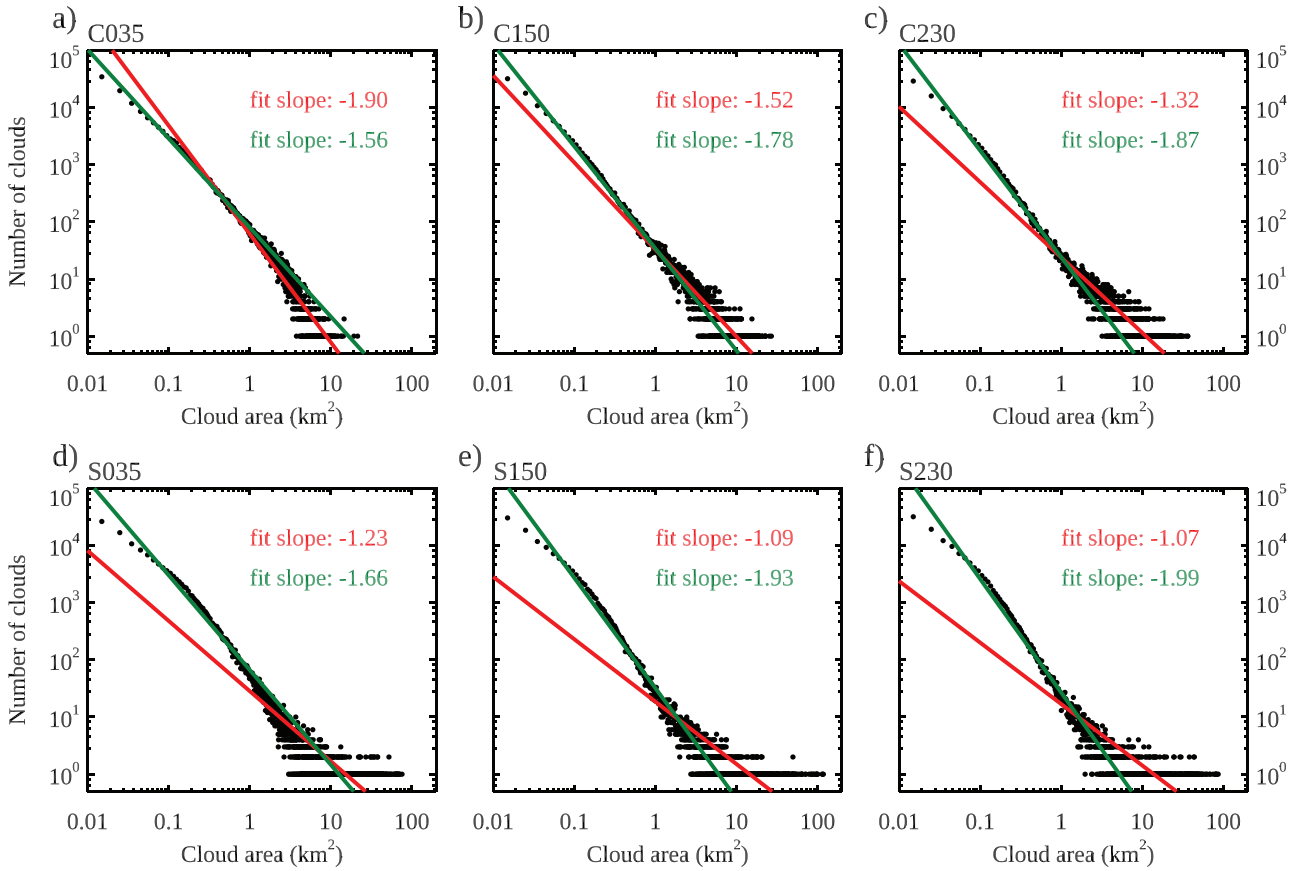

Figure 6. Cloud size distributions calculated based on projected cloud water path for the last 20 hr, sampled every 10 min. Cloudy columns with cloud water path greater than 0.45 g m^{-2} are used, which is ≈ 0.01 g kg^{-1} for a 40-m vertical grid spacing and surface air density. Clouds with bases above 1 km are excluded (the mean cloud base height for all cases is ∼ 700 m, according to Figure 5a). The red and green lines are the best fit power laws obtained based on all clouds, and on clouds with projected area less than 1 km^2, respectively. The corresponding radius for a 1-km^2 cylindrical cloud is approximately 564 m. For the control case, the number of clouds greater than 1 km^2 is 7,100, 4,280, and 3,516 for (a), (b), and (c), respectively. For the shear case, these numbers are 4,963, 2,953, and 2,478 for (d), (e), and (f), respectively.

shear results in a lower cloud top, a slightly lower inversion height, lower liquid water path, and smaller surface precipitation. For the clean cases (C035 and S035), wind shear results in almost the same cloud top (a difference of one vertical grid), a lower inversion height, a larger liquid water path, and larger surface precipitation. Figure 8 presents selected domain-mean profiles (last 20 hr) for the clean and polluted cases. As expected, shear-induced tilting and clustering increase cloud fraction around cloud top and base, respectively (Figure 8d). The polluted cases share similar mean droplet radius, with large drops existing in the overshooting clouds where drizzle/rain drops form (Figures 8c and 8g). Although S230 contains more cloud water mass and number in the overshooting clouds (Figures 8a and 8b), the cloud droplets experience more evaporation due to wind shear and their small size (Figure 8e); this, together with a less efficient collision-coalescence process (based on calculations of the collection tendency; not shown), results in less precipitation (Figures 8g and 8h). Consistent with Asai (1964), evaporation also weakens convection (Figure 8f). Less precipitation and weaker convection in S230 lowers boundary layer height as much as precipitation in C230 does (Figure 8i).

Compared with the polluted cases, the clean cases have much less cloud water in the overshooting clouds (Figure 8a) and larger droplet sizes in the cloud layer (Figure 8c), which generates drizzle/rain that increases as the clouds ascend (Figures 8g and 8h). Although the clean cases share similar cloud water mass, number, and droplet size (Figures 8a, 8b, and 8c), more drizzle/rain is formed for S035 since the clustered clouds are less vulnerable to evaporation and entrainment, allowing more cloud water to be transformed to drizzle/rain. The precipitation leaves more heating in the cloud layer, which results in a lower inversion height (Figure 8i and Table 2).

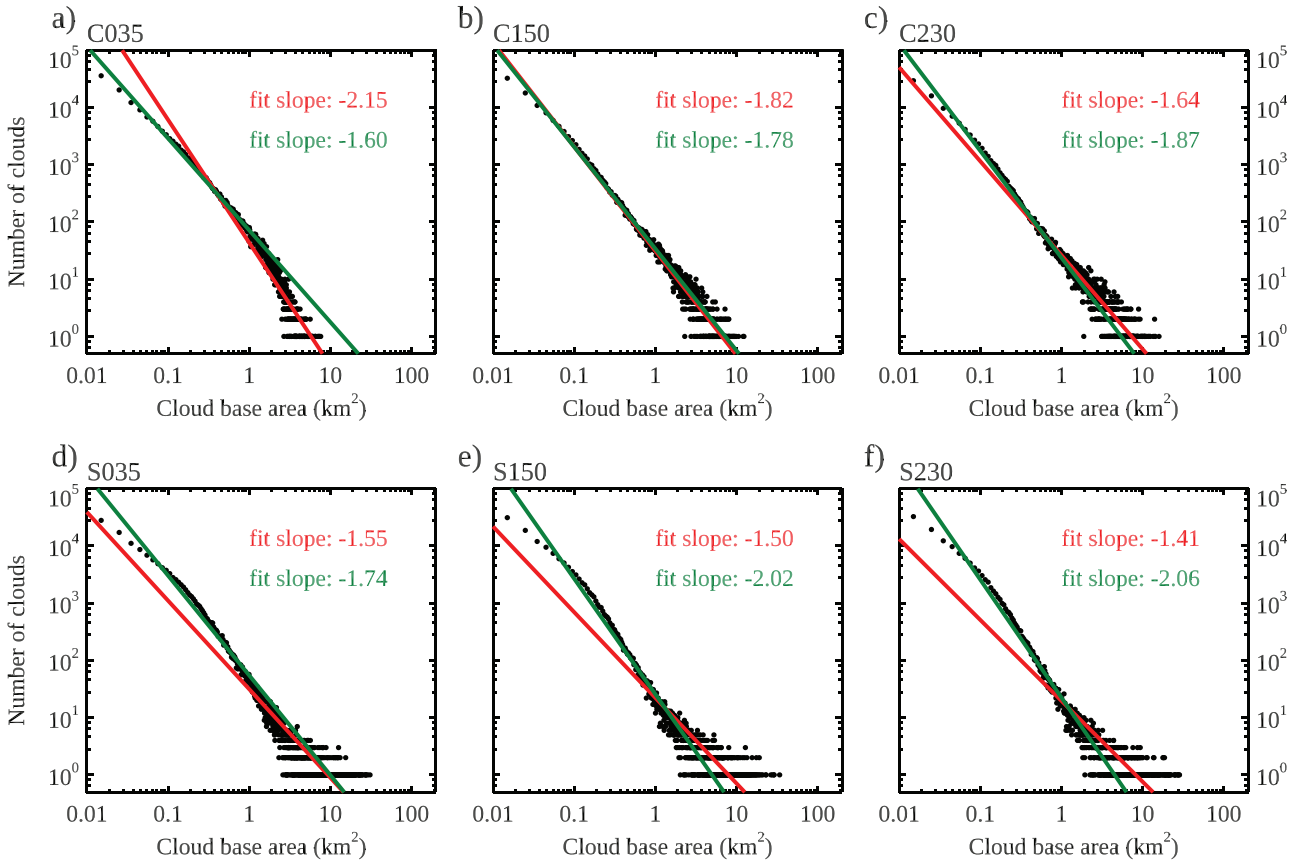

Figure 7. Size distribution of cloud base area. For each cloud, cloud base area is computed by counting pixels with cloud base height below 1 km. The best fit power law is computed for all clouds (red) and for the clouds with projected cloud base area less than 1 km^2 (green). For the control case, the number of clouds greater than 1 km^2 is 4,360, 3,062, and 2,742 for (a), (b), and (c), respectively. For the shear case, these numbers are 3,429, 2,087, and 1,854 for (d), (e), and (f), respectively.

As shown above, tilting, clustering, and precipitation (due to clustering, especially for S035) largely compensate one other and only generate small differences relative to the non-wind shear cases. We now attempt to quantify these compensating effects. For this purpose, a power law model is adapted to describe the relationship between cloud area, a, and cloud depth, d so that $d = \alpha a^{\beta}$ where β is the depth-to-area ratio. When β is small, clouds are required to be wider to reach similar heights. Based on our analysis, tilting leads to smaller β by increasing cloud fraction for a given cloud depth; clustering leads to larger β by deepening clouds for a given cloud area; and precipitation leads to smaller β by limiting vertical development. Since tilting and precipitation tend to decrease β, this measure gives a quantitative estimate of the dominance between clustering and the net effect of tilting and precipitation. Figure 9 shows the two-dimensional histogram for cloud area and its depth with the best fit power law. For all wind shear cases, β is only slightly smaller than for the non-wind shear counterparts. Thus, regardless of N_a, tilting (and precipitation for clean conditions) only just overcomes clustering, to yield lower β.

4.3. Precipitation Cycles in the Aerosol-Buffered System

Although both aerosol and shear have a relatively small effect on the amount of precipitation, of interest is whether the pathways for precipitation formation differ among the cases. For example, deepening, which varies among the cases, enlarges cell sizes, which may generate charge-discharge cycles, as noted in other precipitation studies. Based on LES of BOMEX, Dagan et al. (2018) observed a precipitation cycle with a dominant period of approximately 90 min and a secondary period of 10 min for a range of aerosol number concentrations encompassing those used in our study. Time series analysis showed that the build-up of cloud water leads that of rain water build-up by approximately 20 min. For the same case, Feingold et al. (2017) found an oscillation in the fit slope of CSDs with similar periodicity ($\approx$ 80 and $\approx$ 15 min). These results indicate a physically based link between the precipitation cycle and the cloud size distribution cycle.

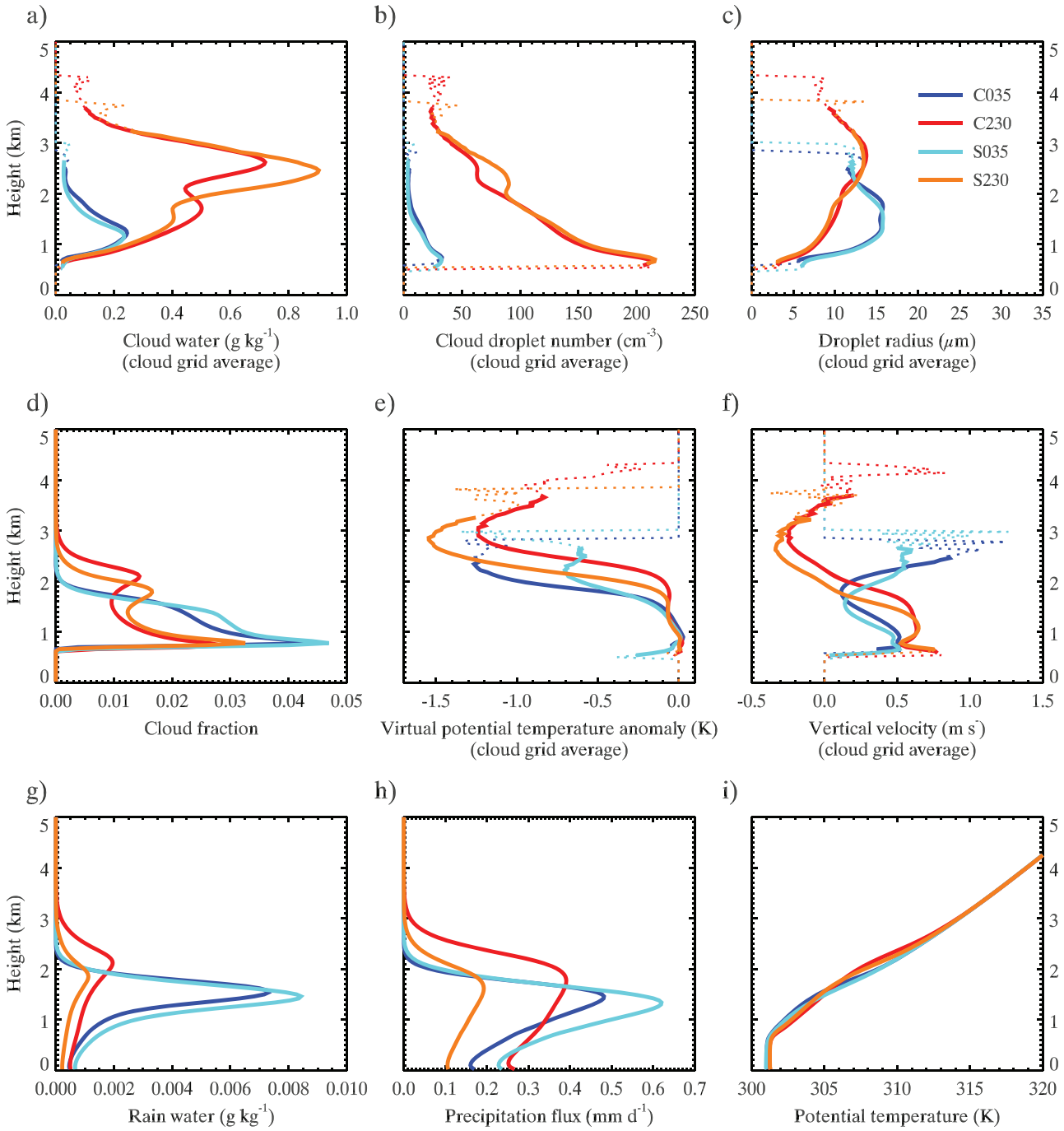

Figure 8. Last 20-hr mean domain mean profile for selected variables for the clean (C035, S035) and polluted (C230, S230) cases. Droplet radius is computed using $r_c = 100\left(\frac{3\overline{q_c}^c}{4\pi\overline{n_c}^c}\right)^{\frac{1}{3}}$, where $\overline{q_c}^c$ is cloudy grid mean cloud water content in g m^{-3} and $\overline{n_c}^c$ is cloudy grid mean cloud droplet number concentration in cm^{-3}. A cloudy grid average profile is given as a conditional mean over all cloudy grids at each level, and each level has to have at least one cloudy grid to be included in the temporal mean. A dotted line is used where the number of samples for mean is less than 10 % of the total number of records over the last 20 hr.

Phase diagrams of the domain mean cloud water path and rain water path for all cases are shown in Figure 10. Expected charge-discharge cycles can be identified, but with clear influence of both aerosol and shear. For low aerosol conditions (particularly C035), only a small part of phase space is covered. The orientation of the cycles is steep, indicating an efficient precipitation process, as might have been anticipated by the widespread rain in Figure 3 (top row). With progressive increases in N_a, more of the phase space is covered, and the orientation of the cycles becomes flatter, as indicated by the linear best fit lines. Thus larger

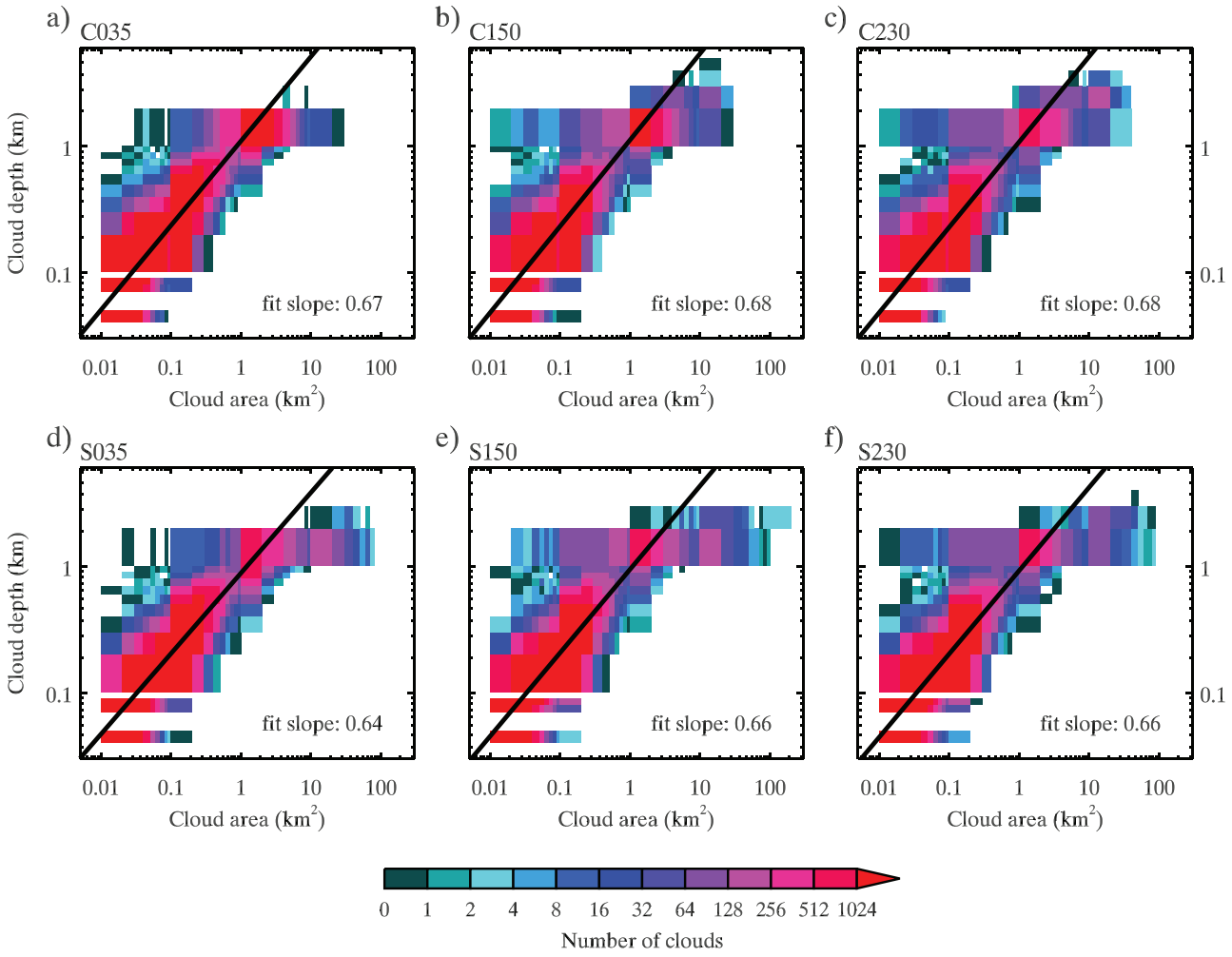

Figure 9. Two-dimensional histogram of cloud area and cloud depth with the best fit power law. The figure is created with the same cloud data used in Figure 6.

increases in cloud water are required to generate rain, that is, precipitation efficiency is reduced. Wind shear has a small effect on the slopes, although interestingly, S230 has a gentler slope than C230 while the S035 and S150 cases have steeper slopes than their C counterparts. This is attributed to a compensation between tilting and clustering, as discussed above, that is, clustering in S035 and S150 creates a more efficient rain process relative to C035 and C150, whereas in S230 tilting reduces efficiency. (See also 8g and 8h.)

Figures 11a and 11b show time series of cloud water path (L_c), rain water path, the fit slope of CSD diagnosed based on all clouds, and the total area of clouds larger than 1 km^2. All simulated cases share somewhat comparable lagged correlations (0.57±0.12; minimum 0.36; maximum 0.77) and lags (11 ± 6 min; minimum 0 min; maximum 20 min) between L_c and the other three variables, as well as surface precipitation rate. The analysis is performed at 10-min output frequency. L_c always leads these variables. The temporal coherence between the CSD cycle and the precipitation cycle supports the notion that precipitation tends to form preferentially in cloud populations comprising large clouds and flatter CSD slopes.

Spectral analysis is utilized to find the dominant period of the precipitation cycle for our simulations. Figures 11c and 11d show raw (10-min interval), low-pass filtered ($\overline{\ }^{\mathrm{lp}}$), and band-pass filtered ($\overline{\ }^{\mathrm{bp}}$) L_c for C035 and S230. The bound of the low-pass filter is a 1-hr period, and the lower (upper) bound of the band-pass filter is 1 hr (2 hr). This band-pass width encompasses the major period of 90 min found by Dagan et al. (2018) and Feingold et al. (2017). $\overline{L_c}^{\mathrm{lp}}$ represents L_c well and the correlation is high — between 0.85 and 0.97 for all six cases. The correlation between L_c and $\overline{L_c}^{\mathrm{bp}}$ is between 0.32 (S230) and 0.69 (C035); it decreases in the presence of wind shear and increased aerosol loading. Thus, for the current simulations, low frequency modes (period greater than 1 hr) are important for the precipitation cycle and more so than modes in the

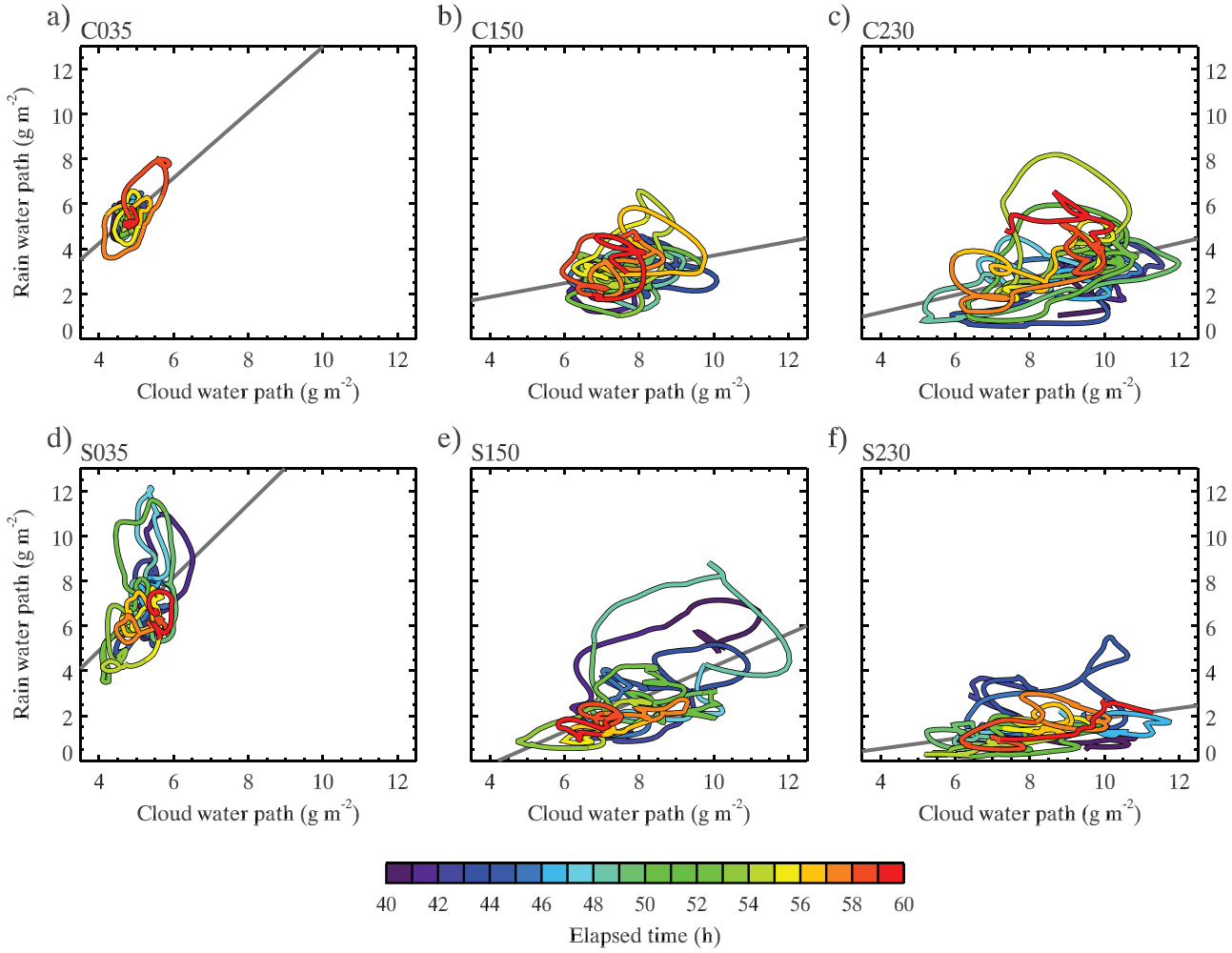

Figure 10. Phase diagram of domain-mean cloud water path and rain water path for the last 20 hr. The diagram is created based on 1-min data, and each hour is indicated with a color. The gray line is the linear least-squares fit line.

1- to 2-h window. That we do not identify a stronger correlation in the 1- to 2-h window as did Dagan et al. (2018) and Feingold et al. (2017) is not surprising, given the much stronger convection in the current case. Nevertheless, we cannot rule out contributions to the low frequency modes from the artificial influences of the doubly periodic boundary conditions and perhaps insufficient domain size for clustered clouds.

Finally, comparison of $\overline{L}_c^{\mathrm{lp}}$ between C035 and S230 (Figures 11c and 11d) suggests that the frequency of the charge-discharge cycle is higher for C035 than S230. As discussed earlier, a combination of microphysical suppression of rain, deepening of clouds, and drier compensating downdrafts likely explains the increasing distances between precipitating areas with progressive increases in aerosol loadings. Thus, the link between the precipitation cycle and the CSD cycle is controlled by the spatial distribution of clouds, which is in turn influenced by the aerosol loading.

5. Summary and Conclusions

An idealized trade wind cumulus case based on the 7SEAS cruise in the Philippines is designed, and LES are performed with a two-moment bin microphysics scheme to examine aerosol-cloud interactions and to investigate the influence of vertical wind shear. For the no-shear case, a 6.5 fold increase in aerosol loading leads to deeper clouds, larger liquid water paths and surface rain, and a small decrease in cloud fraction. To first order, however, the system has a muted response to the very large aerosol perturbation (e.g., Seifert et al., 2015). Cloud deepening is sufficiently large to overcome the microphysical suppression of precipitation. Both cloud deepening and brightening work in unison to create brighter clouds (SWCRE in Table 2).

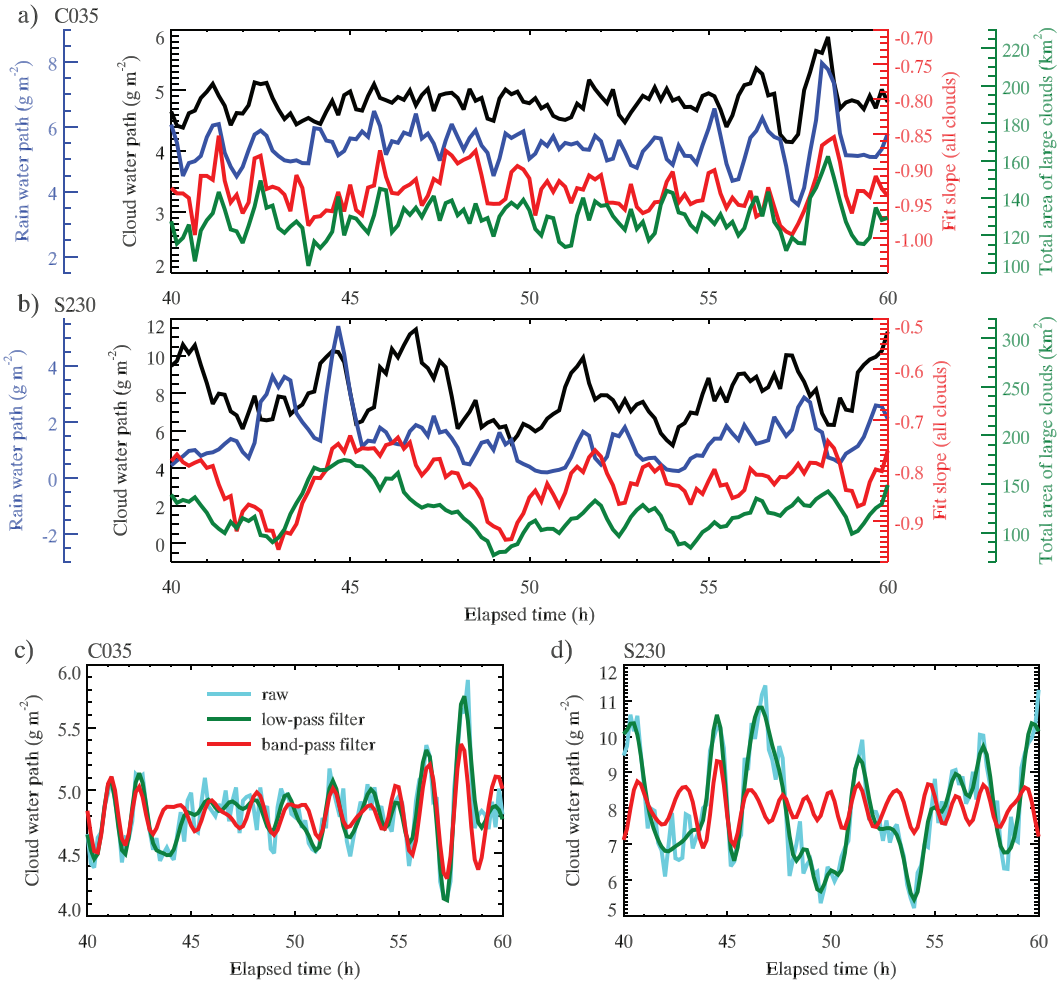

Figure 11. a) and b) show time series of cloud water path (black), rain water path (blue), fit slope of CSD computed for all clouds (red), and total area of large clouds (area larger than 1 km^2) for C035 and S230. c) and d) show time series of raw (light blue), low-pass filtered (green), and band-pass filtered (red) cloud water path for C035 and S230. The threshold for the low-pass filter is 1-hr period, and the lower and upper bounds for the band-pass filter are 1- and 2-hr periods. Time series are based on model output at 10-min resolution.

In the presence of wind shear, cloud deepening in response to aerosol perturbations is weaker and liquid water path and surface rain decrease with increasing aerosol. Cloud fractions, while slightly larger than in the no-shear case, also decrease with increasing aerosol. For all aerosol loadings, SWCRE is somewhat larger than in the no-shear case, mostly because of the higher cloud fractions, but in part because drop concentrations tend to be higher.

Consistent with past studies, wind shear tilts clouds and spreads cloud tops, which increases cloud fraction and evaporation near cloud top. Droplet evaporation is more effective for polluted air. Wind shear is also found to cluster clouds, which increases cloud base area and protects cloud cores (hence leading to an increase in cloud cover). The cloud clustering itself promotes deeper cloud tops and the formation of precipitation, which limits further cloud growth. Increasing aerosol loading also leads to cloud clustering. The differences among simulations are reasonably well explained with tilting, clustering, precipitation, and internal compensations between these processes. The influence of cloud clustering is shown by comparing cloud size distributions based on cloud top projections (CSD) and cloud base projections (CBSD). The analysis reveals that CSDs have more large clouds than CBSDs, that is, that clouds broaden with increasing altitude through the generation of anvils, or via tilting. Both wind shear and aerosol loading modulate CSD and CBSD in the same direction; however, wind shear imposes a greater effect. Lastly, the analysis shows that the effects of tilting are a little larger than those of clustering for the case studied.

Although the very large (factor 6.5) aerosol perturbations and application of vertical wind shear have a relatively small effect on key cloud fields such as surface rain rate (Table 2), the pathways for producing rain differ significantly among the simulations (Figures 10 and 11). Under clean conditions, precipitation efficiency is high, rain is widespread, and small increases in domain-average liquid water path quickly manifest as increases in rain amount. For larger aerosol loadings, precipitation efficiency is lower and rain tends to be confined to large cloud clusters that generate strong outflows and convergence zones, which perpetuate the precipitation (Figures 3 and 4). This can be seen, for example, in the higher amplitude, lower frequency oscillations in Figures 10f and 11d (cf. Figures 10a and 11c, respectively). Thus, strong dynamical modulators in the form of large/deep cloud clusters tend to compensate for microphysical suppression of rain. This is in the spirit of the concept of buffering as described by Stevens and Feingold (2009).

The charge-discharge cycles in cloud water precede those in rain water and surface precipitation by approximately 10 min with a (lagged) correlation of roughly 0.6. This is also true for the fit slope of CSDs and the total area of large clouds (Figure 11). The coherence between the time series of rain and CSDs lends credence to the idea that the similar frequencies in charge-discharge cycles (Dagan et al., 2018) and CSD variability (Feingold et al., 2017) are indeed related. While the aforementioned papers identified a dominant frequency of 80 – 90 min for BOMEX simulations, the period of the precipitation cycle in our deeper cumulus simulations is not exactly captured with periods between 1 and 2 hr, and it is found that inclusion of low frequency modes is important.

There are many reasons to encourage further research to foster understanding of shallow trade cumulus systems. The physical interpretations presented rely on one idealized trade wind cumulus case with limited supporting evidence. Clearly, more case studies are desirable to test our models against a wider variety of observations. The 48 × 48 km domain size may still be too small especially for very clustered cases, which may contain lurking artificial influences on the results, for example, the quantification of the low frequency modes in the precipitation cycle might be artificial. LES is prone to numerical diffusion associated with wind shear. Although the effect of the numerical diffusion is minimized by translating the domain with respect to the initial surface wind and applying rather weak wind shear (albeit consistent with the 7SEAS cruise), the degree of its influence on the results is unknown. Again, more numerical studies of this kind are necessary to confirm the findings and explore further the interplay between trade wind cumulus clouds and wind shear for cloud development and cloud clustering.

Acknowledgments
This work is supported by NOAA's Climate Goal and NASA CAMP^{2}Ex (NNH16ZDA001N; K. S. Schmidt, PI). We thank J. Reid for identifying the 7SEAS event upon which this case study is based. ERA5 data were generated using Copernicus Climate Change Service Information. Neither the European Commission nor the European Centre for Medium-Range Weather Forecasts are responsible for any use that may be made of the Copernicus information or data in this publication. Questions regarding the System for Atmospheric Modeling (SAM) should be directed to M. Khairoutdinov. Data related to this study are available at https://esrl.noaa.gov/csd/groups/csd2/clouds

References

Albrecht, B. A. (1989). Aerosols, cloud microphysics, and fractional cloudiness. *Science*, *245*(4923), 1227. https://doi.org/10.1126/science.245.4923.1227

Asai, T. (1964). Cumulus convection in the atmosphere with vertical wind shear: Numerical experiment. *Journal of the Meteorological Society of Japan (JMSJ)*, *42*(4), 245–259. https://doi.org/10.2151/jmsj1923.42.4_245

Bohren, C. F. (1987). Multiple scattering of light and some of its observable consequences. *American Journal of Physics*, *55*(6), 524–533. https://doi.org/10.1119/1.15109

Boucher, O., Randall, D., Artaxo, P., Bretherton, C., Feingold, G., Forster, P., et al. (2013). *Clouds and aerosols* (pp. 571–658). Cambridge: Cambridge University Press. https://doi.org/10.1017/CBO9781107415324.016

Brown, A. R. (1999). Large-eddy simulation and parametrization of the effects of shear on shallow cumulus convection. *Boundary-Layer Meteorology*, *91*(1), 65–80. https://doi.org/10.1023/A:1001836612775

Clark, T. L. (1974). A study in cloud phase parameterization using the gamma distribution. *Journal of the Atmospheric Sciences*, *31*(1), 142–155. https://doi.org/10.1175/1520-0469(1974)031<0142:ASICPP>2.0.CO;2

Dagan, G., Koren, I., Altaratz, O., & Heiblum, R. H. (2017). Time-dependent, non-monotonic response of warm convective cloud fields to changes in aerosol loading. *Atmospheric Chemistry and Physics*, *17*, 7435–7444. https://doi.org/10.5194/acp-17-7435-2017,aCP

Dagan, G., Koren, I., Kostinski, A., & Altaratz, O. (2018). Organization and oscillations in simulated shallow convective clouds. *Journal of Advances in Modeling Earth Systems*, *10*, 2287–2299. https://doi.org/10.1029/2018MS001416

Deardorff, J. W. (1980). Stratocumulus-capped mixed layers derived from a three-dimensional model. *Boundary-Layer Meteorology*, *18*, 495–527. https://doi.org/10.1007/BF00119502

Durran, D. R. (1991). The third-order Adams-Bashforth method: An attractive alternative to leapfrog time differencing. *Monthly Weather Review*, *119*(3), 702–720. https://doi.org/10.1175/1520-0493(1991)119<0702:TTOABM>2.0.CO;2

Feingold, G., Balsells, J., Glassmeier, F., Yamaguchi, T., Kazil, J., & McComiskey, A. (2017). Analysis of albedo versus cloud fraction relationships in liquid water clouds using heuristic models and large eddy simulation. *Journal of Geophysical Research: Atmospheres*, *122*, 7086–7102. https://doi.org/10.1002/2017JD026467

Feingold, G., Kreidenweis, S. M., Stevens, B., & Cotton, W. R. (1996). Numerical simulations of stratocumulus processing of cloud condensation nuclei through collision-coalescence. *Journal of Geophysical Research*, *101*(D16), 21,391–21,402. https://doi.org/10.1029/96jd01552

Feingold, G., Tzivion, S., & Levin, Z. (1988). Evolution of raindrop spectra. Part I: Solution to the stochastic collection/breakup equation using the method of moments. *Journal of the Atmospheric Sciences*, *45*(22), 3387–3399. https://doi.org/10.1175/1520-0469(1988)045<3387:EORSPI>2.0.CO;2

Hall, W. D. (1980). A detailed microphysical model within a two-dimensional dynamic framework: Model description and preliminary results. *Journal of the Atmospheric Sciences*, *37*(11), 2486–2507. https://doi.org/10.1175/1520-0469(1980)037<2486:ADMMWA>2.0.CO;2

Houze, R. A. (2018). 100 years of research on mesoscale convective systems. *Meteorological Monographs*, *59*, 17.1–17.54. https://doi.org/10.1175/AMSMONOGRAPHS-D-18-0001.1

Iacono, M. J., Delamere, J. S., Mlawer, E. J., Shephard, M. W., Clough, S. A., & Collins, W. D. (2008). Radiative forcing by long-lived greenhouse gases: Calculations with the AER radiative transfer models. *Journal of Geophysical Research*, *113*, D13103. https://doi.org/10.1029/2008JD009944

Jiang, H., Feingold, G., & Koren, I. (2009). Effect of aerosol on trade cumulus cloud morphology. *Journal of Geophysical Research*, *114*(D11), D11209. https://doi.org/10.1029/2009JD011750

Khairoutdinov, M. F., & Kogan, Y. (2000). A new cloud physics parameterization in a large-eddy simulation model of marine stratocumulus. *Monthly Weather Review*, *128*(1), 229–243. https://doi.org/10.1175/1520-0493(2000)128<0229:ANCPPI>2.0.CO;2

Khairoutdinov, M. F., & Randall, D. A. (2003). Cloud resolving modeling of the ARM summer 1997 IOP: Model formulation, results, uncertainties, and sensitivities. *Journal of the Atmospheric Sciences*, *60*(4), 607–625. https://doi.org/10.1175/1520-0469(2003)060<0607:CRMOTA>2.0.CO;2

Koren, I., Dagan, G., & Altaratz, O. (2014). From aerosol-limited to invigoration of warm convective clouds. *Science*, *344*(6188), 1143. https://doi.org/10.1126/science.1252595

Li, Z., Zuidema, P., & Zhu, P. (2014). Simulated convective invigoration processes at trade wind cumulus cold pool boundaries. *Journal of the Atmospheric Sciences*, *71*(8), 2823–2841. https://doi.org/10.1175/JAS-D-13-0184.1

Low, T. B., & List, R. (1982a). Collision, coalescence and breakup of raindrops. Part I: Experimentally established coalescence efficiencies and fragment size distributions in breakup. *Journal of the Atmospheric Sciences*, *39*(7), 1591–1606. https://doi.org/10.1175/1520-0469(1982)039<1591:CCABOR>2.0.CO;2

Low, T. B., & List, R. (1982b). Collision, coalescence and breakup of raindrops. Part II: Parameterization of fragment size distributions. *Journal of the Atmospheric Sciences*, *39*(7), 1607–1619. https://doi.org/10.1175/1520-0469(1982)039<1607:CCABOR>2.0.CO;2

Malkus, J. S. (1952). The slopes of cumulus clouds in relation to external wind shear. *Quarterly Journal of the Royal Meteorological Society*, *78*(338), 530–542. https://doi.org/10.1002/qj.49707833804

Mlawer, E. J., Taubman, S. J., Brown, P. D., Iacono, M. J., & Clough, S. A. (1997). Radiative transfer for inhomogeneous atmospheres: RRTM, a validated correlated-k model for the longwave. *Journal of Geophysical Research*, *102*(D14), 16,663–16,682. https://doi.org/10.1029/97JD00237

Monin, A. S., & Obukhov, A. M. (1954). Basic laws of turbulent mixing in the atmosphere near the ground. *Contribution of Geophysics of the Institute Academy of Sciences USSR*, *24*(151), 163–187.

Morrison, H., Jensen, A. A., Harrington, J. Y., & Milbrandt, J. A. (2016). Advection of coupled hydrometeor quantities in bulk cloud microphysics schemes. *Monthly Weather Review*, *144*(8), 2809–2829. https://doi.org/10.1175/MWR-D-15-0368.1

Mülmenstädt, J., & Feingold, G. (2018). The radiative forcing of aerosol-cloud interactions in liquid clouds: Wrestling and embracing uncertainty. *Current Climate Change Reports*, *4*(1), 23–40. https://doi.org/10.1007/s40641-018-0089-y

Neggers, R. A. J., Griewank, P. J., & Heus, T. (2019). Power-law scaling in the internal variability of cumulus cloud size distributions due to subsampling and spatial organization. *Journal of the Atmospheric Sciences*, *76*, 1489–1503. https://doi.org/10.1175/JAS-D-18-0194.1

Neggers, R. A. J., Jonker, H. J. J., & Siebesma, A. P. (2003). Size statistics of cumulus cloud populations in large-eddy simulations. *Journal of the Atmospheric Sciences*, *60*(8), 1060–1074. https://doi.org/10.1175/1520-0469(2003)60<1060:SSOCCP>2.0.CO;2

Newman, M. E. J. (2005). Power laws, Pareto distributions and Zipf's law. *Contemporary Physics*, *46*(5), 323–351. https://doi.org/10.1080/00107510500052444

Nuijens, L., & Stevens, B. (2012). The influence of wind speed on shallow marine cumulus convection. *Journal of the Atmospheric Sciences*, *69*(1), 168–184. https://doi.org/10.1175/JAS-D-11-02.1

Ochs, H. T., Czys, R. R., & Beard, K. V. (1986). Laboratory measurements of coalescence efficiencies for small precipitation drops. *Journal of the Atmospheric Sciences*, *43*(3), 225–232. https://doi.org/10.1175/1520-0469(1986)043<0225:LMOCEF>2.0.CO;2

Ovtchinnikov, M., & Easter, R. C. (2009). Nonlinear advection algorithms applied to interrelated tracers: Errors and implications for modeling aerosol–cloud interactions. *Monthly Weather Review*, *137*(2), 632–644. https://doi.org/10.1175/2008MWR2626.1

Reid, J. S., Lagrosas, N. D., Jonsson, H. H., Reid, E. A., Atwood, S. A., Boyd, T. J., et al. (2016). Aerosol meteorology of Maritime Continent for the 2012 7SEAS southwest monsoon intensive study—Part 2: Philippine receptor observations of fine-scale aerosol behavior. *Atmospheric Chemistry and Physics*, *16*, 14,057–14,078. https://doi.org/10.5194/acp-16-14057-2016

Schlemmer, L., & Hohenegger, C. (2014). The formation of wider and deeper clouds as a result of cold-pool dynamics. *Journal of the Atmospheric Sciences*, *71*, 2842–2858. https://doi.org/10.1175/JAS-D-13-0170.1

Seifert, A., & Heus, T. (2013). Large-eddy simulation of organized precipitating trade wind cumulus clouds. *Atmospheric Chemistry and Physics*, *13*, 5631–5645. https://doi.org/10.5194/acp-13-5631-2013

Seifert, A., Heus, T., Pincus, R., & Stevens, B. (2015). Large-eddy simulation of the transient and near-equilibrium behavior of precipitating shallow convection. *Journal of Advances in Modeling Earth Systems*, *7*, 1918–1937. https://doi.org/10.1002/2015MS000489

Siebesma, A. P., Bretherton, C. S., Brown, A., Chlond, A., Cuxart, J., Duynkerke, P. G., et al. (2003). A large eddy simulation intercomparison study of shallow cumulus convection. *Journal of the Atmospheric Sciences*, *60*(10), 1201–1219. https://doi.org/10.1175/1520-0469(2003)60<1201:ALESIS>2.0.CO;2

Stevens, B., & Feingold, G. (2009). Untangling aerosol effects on clouds and precipitation in a buffered system. *Nature*, *461*, 607.

Stevens, B., Feingold, G., Cotton, W. R., & Walko, R. L. (1996). Elements of the microphysical structure of numerically simulated nonprecipitating stratocumulus. *Journal of the Atmospheric Sciences*, *53*(7), 980–1006. https://doi.org/10.1175/1520-0469(1996)053<0980:EOTMSO>2.0.CO;2

Tompkins, A. M. (2001). Organization of tropical convection in low vertical wind shears: The role of cold pools. *Journal of the Atmospheric Sciences*, *58*(13), 1650–1672. https://doi.org/10.1175/1520-0469(2001)058<1650:OOTCIL>2.0.CO;2

Twomey, S. (1977). The influence of pollution on the shortwave albedo of clouds. *Journal of the Atmospheric Sciences*, *34*(7), 1149–1152. https://doi.org/10.1175/1520-0469(1977)034<1149:TIOPOT>2.0.CO;2

Tzivion, S., Feingold, G., & Levin, Z. (1987). An efficient numerical solution to the stochastic collection equation. *Journal of the Atmospheric Sciences*, *44*(21), 3139–3149. https://doi.org/10.1175/1520-0469(1987)044<3139:AENSTT>2.0.CO;2

Vogel, R., Nuijens, L., & Stevens, B. (2016). The role of precipitation and spatial organization in the response of trade-wind clouds to warming. *Journal of Advances in Modeling Earth Systems*, *8*, 843–862. https://doi.org/10.1002/2015MS000568

Xue, H., & Feingold, G. (2006). Large-eddy simulations of trade wind cumuli: Investigation of aerosol indirect effects. *Journal of the Atmospheric Sciences*, *63*(6), 1605–1622. https://doi.org/10.1175/JAS3706.1

Xue, H., Feingold, G., & Stevens, B. (2008). Aerosol effects on clouds, precipitation, and the organization of shallow cumulus convection. *Journal of the Atmospheric Sciences*, *65*(2), 392–406. https://doi.org/10.1175/2007JAS2428.1

Yamaguchi, T., Randall, D. A., & Khairoutdinov, M. F. (2011). Cloud modeling tests of the ULTIMATE-MACHO scalar advection scheme. *Monthly Weather Review*, *139*(10), 3248–3264. https://doi.org/10.1175/mwr-d-10-05044.1

van Zanten, M. C., Stevens, B. B., Nuijens, L., Siebesma, A. P., Ackerman, A., Burnet, F., et al. (2011). Controls on precipitation and cloudiness in simulations of trade-wind cumulus as observed during RICO. *Journal of Advances in Modeling Earth Systems*, *3*, M06001. https://doi.org/10.1029/2011ms000056

Zuidema, P., Li, Z., Hill, R. J., Bariteau, L., Rilling, B., Fairall, C., et al. (2012). On trade wind cumulus cold pools. *Journal of the Atmospheric Sciences*, *69*(1), 258–280. https://doi.org/10.1175/JAS-D-11-0143.1

Zuidema, P., Torri, G., Muller, C., & Chandra, A. (2017). A survey of precipitation-induced atmospheric cold pools over oceans and their interactions with the larger-scale environment. *Surveys in Geophysics*, *38*(6), 1283–1305. https://doi.org/10.1007/s10712-017-9447-x